RSC Advances

ROYAL SOCIETY OF CHEMISTRY

PAPER

View Article Online
View Journal | View Issue

Cite this: *RSC Adv.*, 2026, **16**, 16954

Regulating the metal-insulator transition of $REBaCo_2O_{5+\delta}$ combining RE-substitution and anion control

Fang Zhang,†[a] Yuchen Cui,†[b] Jingxin Gao,[b] Hao Zhang,[b] Yi Bian,[b] Chen Liu,[c] Nuofu Chen*[a] and Jikun Chen *[b]

Received 6th January 2026
Accepted 10th March 2026

DOI: 10.1039/d6ra00137h

rsc.li/rsc-advances

Although an intriguing metal-insulator transition (MIT) stemming from spin-state transition was discovered for cobaltite double-perovskites ($REBaCo_2O_{5+\delta}$), its regulatory mechanism is yet unclear owing to the intertwined dual-determinants from cationic and anionic perspectives. Herein, we demonstrate that the occurrence of abrupt MIT for $REBaCo_2O_{5+\delta}$ relies on the synergistic coordination between the RE ionic-radius-induced CoO_6 octahedral distortion and the oxygen-vacancy-modulated Co valence-state for low structural symmetry. A gradual shift in the transportation behavior from metal to insulator is observed for $REBaCo_2O_{5+\delta}$ synthesized in air with REs from Pr to Ho, while the MIT emerges for middle REs (*e.g.*, Sm, Eu, Gd and Tb). Nevertheless, the MIT was could be further extended to more RE compositions from an anionic perspective by annealing the insulating (RE: Dy and Ho) or metallic (RE: Pr and Nd) $REBaCo_2O_{5+\delta}$ at MPa-high oxygen or nitrogen pressure, respectively. Further estimation the oxygen composition *via* their thermopowers indicates that their MIT behaviors were coincide with a narrow distribution of δ around 0.5 and descendent structural symmetry towards *Pmmm* from *P*4/*mmm*. This unveils the distinctiveness in spin-state transition-driven MIT compared to the Bloch–Wilson, Mott, or Peierls transitions, providing a versatile platform for fundamental explorations beyond conventional correlated electron systems.

1. Introduction

Strongly correlated oxides exhibit complex interactions among the charge, spin, orbital, and lattice degrees of freedom, giving rise to intriguing phenomena, such as the metal-insulator transition (MIT),[1–3] high-temperature superconductivity,[4,5] and colossal magnetoresistance (CMR).[6] Typically, the A-site ordered cobaltite double perovskites with oxygen deficiency ($REBaCo_2O_{5+\delta}$) exhibit a complex electronic phase diagram, stemming from the variations in electron orbital configurations among $t_{2g}^6e_g^0$ ($S=0$), $t_{2g}^5e_g^1$ ($S=1$) and $t_{2g}^4e_g^2$ ($S=2$).[7,8] This endows MIT behaviors to $REBaCo_2O_{5+\delta}$, the mechanism of which differs from the well-known Bloch–Wilson, Mott, and Peierls transitions. $REBaCo_2O_{5+\delta}$ exhibits a 112-type cation composition, showing $[CoO_2]$–$[BaO]$–$[CoO_2]$–$[REO_x]$ stacking units.[9] The relatively large ionic radius of Ba causes A-site ordering, such that the rare-earth and alkaline-earth cations are located in distinct crystallographic layers.[10] It is noteworthy that under identical synthesis conditions, the symmetry in the crystal structure of $REBaCo_2O_{5+\delta}$ varies depending on the type of RE. For example, under air conditions at 1100 °C, the synthesized $REBaCo_2O_{5+\delta}$ compounds exhibit different space groups depending on the rare-earth elements.[11,12] Light $RE_LBaCo_2O_{5+\delta}$ (RE_L: Pr and Nd) and heavy $RE_LBaCo_2O_{5+\delta}$ (RE_H: Dy and Ho) crystallize in the space group *P*4/*mmm*, while mid $RE_LBaCo_2O_{5+\delta}$ (RE_M: Sm, Eu, Gd, and Tb) crystallizes in the space group *Pmmm*.[13] Also, the oxygen composition (δ = 0–1) could be further tuned by post annealing in an oxygen containing or reducing atmosphere,[14] leading to variations in the valence state of Co and thereby d-orbital filling. Owing to such dual degrees of freedom in tuning the d-orbital configuration, the critical temperature associated with MIT (T_{MIT}) of $REBaCo_2O_{5+\delta}$ shows a more complicated variation with the ionic radius of the rare-earth (r_{RE}), compared to the monotonic tendency as observed for perovskites such as $RENiO_3$ (ref. 1) and $RECoO_3$.[2] This establishes an ideal material platform to further explore the inherent connections among the charge, spin, orbital, and lattice under more crystal fields beyond conventional 113-type perovskites.

To gain a better fundamental understanding of the determinant of the orbital configuration of $REBaCo_2O_{5+\delta}$, it is urgent to decouple the respective influence from the perspectives

[a]*School of Renewable Energy, North China Electric Power University, Beijing 102206, China. E-mail: nfchen@ncepu.edu.cn*

[b]*School of Materials Science and Engineering, University of Science and Technology Beijing, Beijing 100083, China. E-mail: jikunchen@ustb.edu.cn*

[c]*Beijing Synchrotron Radiation Facility, Institute of High Energy Physics, Chinese Academy of Sciences, Beijing 100049, China*

† F. Zhang and Y. Cui contribute equally.

associated with the cation (*e.g.*, rare-earth compositions) and anion (*e.g.*, oxygen vacancy). Although decreasing r_{RE} was known to distort the CoO_6 octahedra more to reduce the orbital overlapping between O-2p and Co-3d, it meanwhile exacerbated the formation of oxygen vacancies within $REBaCo_2O_{5+\delta}$ that reduces the valence of Co. This is attributed to the intermediate valence state of Co within $REBaCo_2O_{5+\delta}$ that is susceptible to both structural distortions and reaction atmospheres. Consequently, such entangled regulations from both the band gap regulation and orbital filling control impedes further comprehending the relationship among the charge, spin, orbital, and lattice underlying the MIT behavior of $REBaCo_2O_{5+\delta}$. To address this core issue, further systematic studies of the electronic structure and transportation properties of the as-synthesized $REBaCo_2O_{5+\delta}$ sample at various oxygen partial pressures (p_{O_2}) are needed.

In this work, we disentangle the role of RE ionic radius-induced CoO_6 octahedral distortion and oxygen vacancy-modulated Co valence state in the MIT behavior of $REBaCo_2O_{5+\delta}$ by their first synthesis in air followed by post-annealing in various atmospheres, covering a large variety of RE compositions. The resulting variations in electronic transportation properties (*e.g.*, resistivity and thermopower) were systematically investigated, and further related to the ones observed in crystal and electronic structures. We highlight the synergistic coordination between the RE ionic radius and the oxygen composition, resulting in the emergence of abrupt MIT for $REBaCo_2O_{5+\delta}$, unveiling the distinctiveness in spin-state transition-driven MIT, compared to the Bloch–Wilson, Mott, or Peierls transitions.

2. Experimental

2.1. Sample preparation

The powders of $REBaCo_2O_{5+\delta}$ were prepared by the solid-state reactions between RE_2O_3 (RE = La, Pr, Nd, Sm, Eu, Gd, Tb, Dy, Ho, and Er), $BaCO_3$, and Co_3O_4 as starting materials. The stoichiometric mixtures of the starting materials were ground thoroughly in an agate mortar and cold-pressed, followed by solid-phase reaction sintering at 1100 °C in an air atmosphere for 12 hours. The powders were pressed into pellets using a mold, and sintered into pellets at 1100 °C in air. Some selected samples were further annealed at 300 °C and 5 MPa oxygen for 24 hours, or annealed at 300 °C in a nitrogen flow for 12 hours. The temperature coefficient of resistance and thermoelectric power (S) was measured in sequence.

2.2. Characterizations

The crystal structures of the as-grown $REBaCo_2O_{5+\delta}$ powders were analyzed by X-ray diffraction (XRD) using a RIGAKU Ultima IV (Cu K_α, $\lambda = 0.1541$ nm). The as-sintered $REBaCo_2O_{5+\delta}$ pellets were first processed into strip-shaped samples with dimensions of $3 \times 10 \times 2$ mm^3, and the electrical resistivities of these samples were measured *via* the four-terminal collinear method using a commercial CTA setup. To investigate how different A-site elements and oxygen pressure affect the electronic structure of $REBaCo_2O_{5+\delta}$, the NEXAFS analysis was performed to probe the O-K and Co-L edges of the $REBaCo_2O_{5+\delta}$ (RE = Sm, Gd, Tb, and Ho) powders sintered in air at the 4B9B station (λ = 130–360 nm; spot size < 2×0.8 mm^2) of the Beijing Synchrotron Radiation Facility (BSRF). The energy shift was calibrated by the Au foil. S was characterized using an electronic and thermal transport measurement system *via* the quasi-steady-state method. The samples were positioned between two heat baths separated by a 4 mm gap. One side acted as a heat sink, which was controlled to maintain the set temperature with an error margin of less than 0.1 K. The other heat bath functioned as a heat source equipped with a heater.

3. Results and discussions

3.1. Structure and transport properties of $REBaCo_2O_{5+\delta}$ synthesized in air

We first investigated the influence of r_{RE} on the crystal structures and electrical transportation performances of $REBaCo_2O_{5+\delta}$ as synthesized in air at the same temperature (*e.g.*, 1100 °C). The representative crystal structures of $REBaCo_2O_{5+\delta}$ are illustrated in Fig. 1(a). From left to right, the structures of $REBaCo_2O_{5+\delta}$ containing light (RE_L: Pr and Nd), middle (RE_M: Sm, Eu, Gd, and Tb) and heavy (RE_H: Dy and Ho) rare-earth elements are illustrated. $RE_MBaCo_2O_{5+\delta}$ (space group: *Pmmm*) manifests a lower symmetry in crystal structures than $RE_LBaCo_2O_{5+\delta}$ and $RE_HBaCo_2O_{5+\delta}$ (space group: *P*4/*mmm*). Fig. 1(b) shows the XRD patterns and their Rietveld refinements of the as-synthesized $REBaCo_2O_{5+\delta}$ sample (RE = La, Pr, Gd, Ho, and Er) in air. More XRD patterns and detailed refinement results of other rare earths are shown in Tables S1, S2 and Fig. S1. It can be seen that for varying RE from Pr to Ho, expected double-perovskite structures of $REBaCo_2O_{5+\delta}$ are observed, without the presence of impurities. In contrast, it is not capable of synthesizing $ErBaCo_2O_{5+\delta}$ owing to the further reduction in r_{RE}, which is similar to the case of $REBaFe_2O_{5+\delta}$.[15]

Fig. 1(c) shows the lattice parameters of $REBaCo_2O_{5+\delta}$ from the Rietveld refinement as a function of r_{RE}, where the solid symbols represent our experimental data and the hollow symbols represent the data from references.[11,14] Notably, the refinement of $RE_LBaCo_2O_{5+\delta}$ and $RE_HBaCo_2O_{5+\delta}$ was performed using the *P*4/*mmm* space group, while that of $RE_MBaCo_2O_{5+\delta}$ was performed using the *Pmmm* space group. It more clearly demonstrates the diversity in 2a and b for $REBaCo_2O_{5+\delta}$ containing middle rare-earth elements, giving rise to a descended symmetry in the structure. We also tried to perform refinement for $REBaCo_2O_{5+\delta}$ containing the heavy or light rare-earth elements using the *Pmmm* space group (see more details in Table S1 and Fig. S2), the operation of which results in similar magnitudes in 2a and b. Our results are in consistency with the previous reports by T. V. Aksenova *et al.*,[11] T. Dasgupta *et al.*,[16] and I. O. Troyanchuk *et al.*[13]

The temperature dependence of resistivity was further measured for the as-synthesized $REBaCo_2O_{5+\delta}$, as shown in Fig. 2(a). It can be seen that the light rare-earth element-containing samples (RE_L = Pr and Nd) exhibit metallic behavior, while the heavy rare-earth element-containing

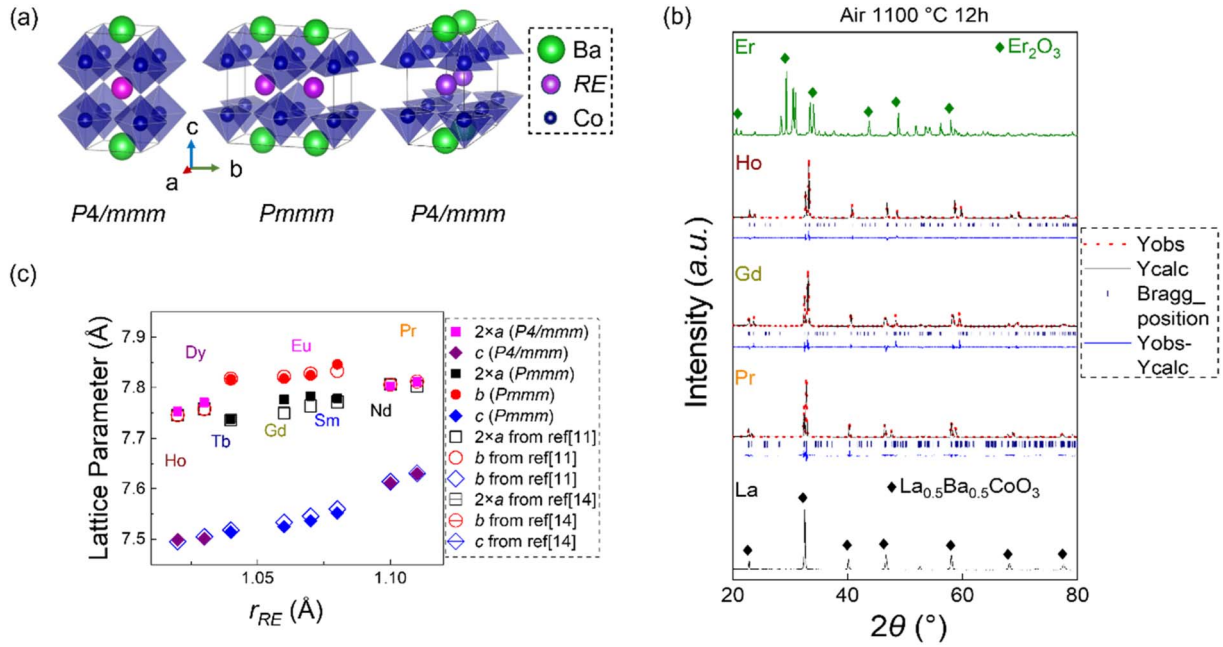

Fig. 1 (a) Illustration of the crystal structure of $REBaCo_2O_{5+\delta}$ (RE represents rare-earth elements) containing light (Pr and Nd), middle (Sm, Eu, Gd and Tb) and heavy (Dy and Ho) rare-earth elements, where RE, Ba and Co atoms are represented by purple, green, and dark blue, respectively. From left to right, there are schematic diagrams of the structures of $RE_LBaCo_2O_{5+\delta}$ (RE_L = Pr and Nd), $RE_MBaCo_2O_{5+\delta}$ (RE_M = Sm, Eu, Gd and Tb), and $RE_HBaCo_2O_{5+\delta}$ (RE_H = Dy and Ho). (b) X-ray diffraction (XRD) patterns of $REBaCo_2O_{5+\delta}$ synthesized *via* a solid-state reaction in air. (c) Lattice parameters of the as-synthesized $REBaCo_2O_{5+\delta}$ sample (solid symbols) plotted as a function of the ionic radius of rare-earth elements compared to the previous reports (hollow symbols).[11,14] The $RE_LBaCo_2O_{5+\delta}$ and $RE_HBaCo_2O_{5+\delta}$ samples were refined using the *P4/mmm* space group, while the $RE_MBaCo_2O_{5+\delta}$ sample was refined using the *Pmmm* space group.

samples (RE_H = Dy and Ho) show semiconducting behavior. More intriguingly, abrupt MITs are observed for the middle rare-earth element-containing $RE_MBaCo_2O_{5+\delta}$ (RE_M = Sm, Eu, Gd, and Tb), which coincides with a low symmetry in their ground-state crystal structures (*e.g.*, *Pmmm* compared to *P4/mmm*), in agreement with the previous observations.

The variations in carrier types and concentrations of the air-synthesized $REBaCo_2O_{5+\delta}$ with various rare-earth compositions were also indicated by their different temperature dependence of S, as shown in Fig. 2(b). At low temperatures (*e.g.*, 100 K), the absolute magnitude $|S|$ shows an increasing tendency along the lanthanide sequence with reduced r_{RE} until Tb. However, when the ionic radius continues to decrease, the S of $DyBaCo_2O_{5+\delta}$ begins to decrease. It is interesting to note that $HoBaCo_2O_{5+\delta}$ manifests a negative magnitude in S indicating the electron as a major carrier, which differs from the rest $REBaCo_2O_{5+\delta}$. With an elevation in temperature, a reducing tendency is generally observed for the $|S|$ of all $REBaCo_2O_{5+\delta}$, and this is in agreement with their negative temperature dependence in resistivity. Abrupt transitions are observed in $|S|$–T for $RE_MBaCo_2O_{5+\delta}$ in the range of 330–360 K, and this is in consistency with their MIT behaviors. In contrast, a gradual reduction in $|S|$ is observed for $DyBaCo_2O_{5+\delta}$ and $HoBaCo_2O_{5+\delta}$ with the heavier rare-earth composition showing insulating transportation behavior, while $PrBaCo_2O_{5+\delta}$ shows a small magnitude in $|S|$ with low-temperature dependences owing to the metallic transportation behavior.

The above observation is in consistency with the previous reports, and was attributed to the variation in oxygen stoichiometry across rare-earth substitutions. According to references,[16,17] this is likely due to its oxygen content δ being closest to, and slightly greater than, 0.5. In fact, the δ value of $TbBaCo_2O_{5+\delta}$ synthesized in this experiment is approximately 0.53.[18] In contrast, the δ value of other $REBaCo_2O_{5+\delta}$ compounds (RE ≠ Tb) deviates more significantly from 0.5, with δ in $PrBaCo_2O_{5+\delta}$ around 0.7,[14] in $SmBaCo_2O_{5+\delta}$ around 0.61 (ref. 19) and in $DyBaCo_2O_{5+\delta}$ around 0.3.[14]

The electronic structure of the as-synthesized $REBaCo_2O_{5+\delta}$ sample with various rare-earth compositions (RE = Sm, Tb, and Ho) was further probed by the near-edge X-ray absorption fine structure (NEXAFS), and their Co L-edge spectrum is shown in Fig. 2(c). Compared with the Co L_3-edge spectra of Co^{2+}, Co^{3+}, and Co^{4+} in reference,[20] Co is predominantly in the +3 oxidation state across all four samples, with no noticeable presence of Co^{2+} or Co^{4+}. This suggests that, despite varying δ in the $REBaCo_2O_{5+\delta}$ samples synthesized in air, the structural and unit cell differences stabilize Co near the +3 oxidation state. Furthermore, the A peak position for all samples is consistent at ~780.4 eV, confirming that the oxidation state of Co remains largely unchanged (higher oxidation states shift the A peak to higher energies). The ref. 19 indicates that $SmBaCo_2O_{5+\delta}$, with a δ value of approximately 0.61 after sintering in air at 1100 °C, has an average Co oxidation state of 3.11, suggesting the presence of Co^{4+}. For $HoBaCo_2O_{5+\delta}$, δ is typically around 0.3,[14]

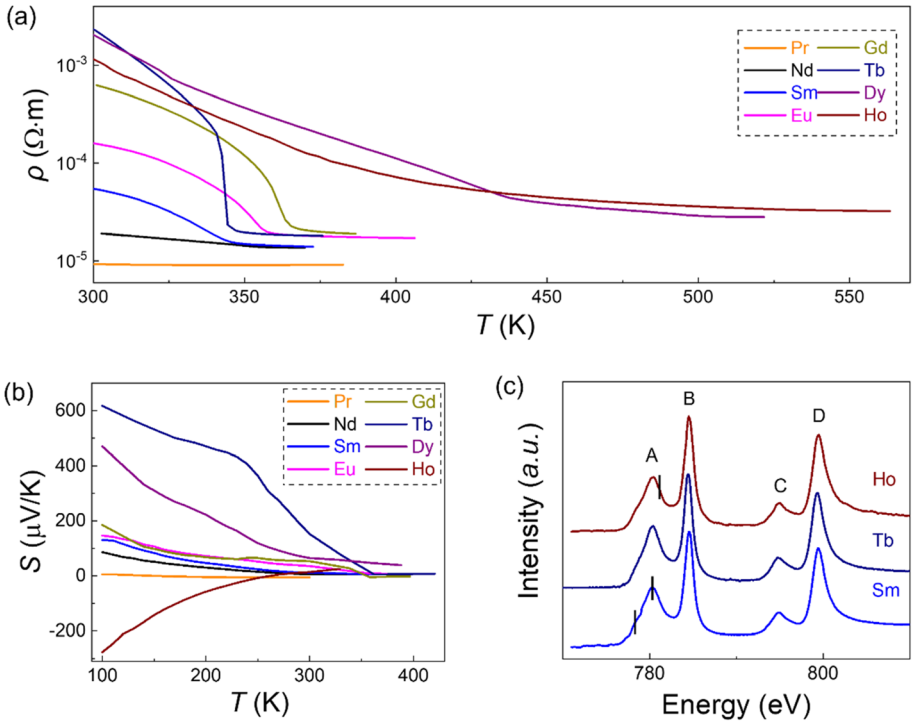

Fig. 2 (a) Temperature dependence of resistivity measured for $REBaCo_2O_{5+\delta}$. (b) Temperature dependence of thermoelectric power in $REBaCo_2O_{5+\delta}$. (c) Co-L edge near-edge X-ray absorption fine structure (NEXAFS) at room temperature.

resulting in an average Co oxidation state of 2.8, which indicates the presence of Co^{2+}.

In contrast to $REBaCo_2O_{5+\delta}$ (RE = Tb and Ho), $SmBaCo_2O_{5+\delta}$ shows a distinct small peak at the left edge of the A peak, corresponding to high-spin Co^{3+} (HS Co^{3+}) as identified in ref. 21–23, while other samples predominantly exhibit intermediate-spin (IS Co^{3+}) or low-spin Co^{3+} (LS Co^{3+}). This is consistent with $SmBaCo_2O_{5+\delta}$ exhibiting metallic-like resistivity (5.5×10^{-5} Ω m) at room temperature, while the other $REBaCo_2O_{5+\delta}$ samples show higher resistivity characteristic of semiconductors. Additionally, $HoBaCo_2O_{5+\delta}$ displays a small peak at the right shoulder of the A peak, corresponding to LS Co^{3+}, consistent with its semiconducting behavior at room temperature.

3.2. Further regulating oxygen composition within $REBaCo_2O_{5+\delta}$ *via* post-annealing in MPa-high oxygen or nitrogen pressure

It is worth noticing that rare-earth substitutions within $REBaCo_2O_{5+\delta}$ as synthesized in air will not only structurally alter the distortion in the CoO_6 octahedra but also vary the oxygen composition (δ). According to the previous reports,[11,14] a higher amount of oxygen vacancies are expected for $REBaCo_2O_{5+\delta}$ as synthesized in air along the lanthanide series, *e.g.*, $\delta > 0.6$ for $RE_LBaCo_2O_{5+\delta}$, $\delta \approx 0.5$ ($0.45 < \delta \leq 0.6$) for $RE_MBaCo_2O_{5+\delta}$, and $\delta < 0.45$ for $RE_HBaCo_2O_{5+\delta}$. To further adjust the oxygen composition of the as-synthesized $REBaCo_2O_{5+\delta}$ sample in air, post-annealing was done at either MPa-high oxygen or nitrogen pressure at 300 °C.

Fig. 3(a) shows the powder XRD pattern of $REBaCo_2O_{5+\delta}$ (RE = Gd, Tb, Dy, and Ho) after oxygen annealing, the process of which results in the broadening of diffraction peaks (see Fig. S3) without introducing secondary phases. The variation in the magnitudes of their lattice parameters was further determined by the Rietveld refinement (see more details in Table S3 and Fig. S4), as plotted as a function of r_{RE} in Fig. 3(b). It clearly demonstrates a symmetry descending in the structure of heavy rare-earth element-containing $REBaCo_2O_{5+\delta}$ (RE: Dy and Ho) from the tetragonal (*P4/mmm*) to the orthorhombic (*Pmmm*) structure, owing to post-annealing at MPa-high oxygen pressures. It is also interesting to note that pronounced MIT behaviors manifest in both $DyBaCo_2O_{5+\delta}$ and $HoBaCo_2O_{5+\delta}$ upon post-annealing at high-oxygen pressures, as shown in Fig. 3(c) and S7(a). This feature corresponds to a decrease in the symmetry of $REBaCo_2O_{5+\delta}$ (RE: Dy and Ho). After oxygen annealing, the phase transition of $GdBaCo_2O_{5+\delta}$ disappears, which is associated with the increase in δ of $GdBaCo_2O_{5+\delta}$ after annealing, leading to a deviation of the Co oxidation state from +3.

Fig. 3(d) shows the temperature dependence of S of $REBaCo_2O_{5+\delta}$ (RE = Gd, Tb, Dy, and Ho) with middle and heavy rare-earth compositions after annealing at MPa-high oxygen pressure to compensate their oxygen composition. It can be seen that the oxygen annealing converted the previously negative magnitude in S for $HoBaCo_2O_{5+\delta}$ towards positive magnitudes. Compared to their air-synthesized counterparts, the magnitude of $|S|$ of all $REBaCo_2O_{5+\delta}$ decreases at 100 K, indicating that after oxygen doping, the δ value deviates from 0.5 (as reported in the literature,[17] where it is known that the absolute

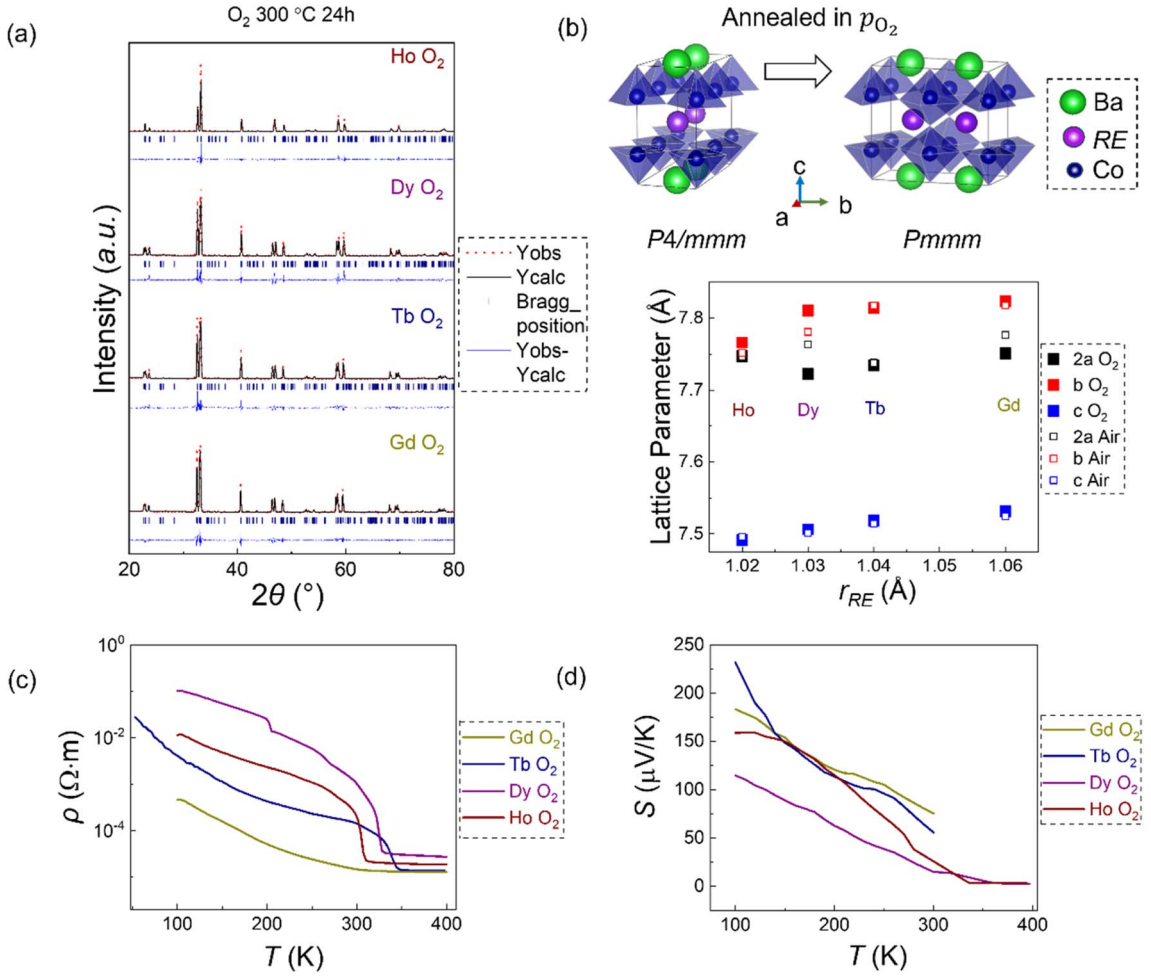

Fig. 3 (a) X-ray diffraction (XRD) patterns of the powder of $REBaCo_2O_{5+\delta}$ annealed in 5 MPa oxygen for 24 hours at 300 °C. (b) Top image illustrates the crystal structure of $REBaCo_2O_{5+\delta}$ (RE represents rare-earth elements), where RE, Ba, and Co atoms are represented by purple, green, and dark blue, respectively. On the left is a schematic of the structure of $RE_HBaCo_2O_{5+\delta}$ synthesized in air, and on the right is a schematic of the structure of $RE_HBaCo_2O_{5+\delta}$ annealed in oxygen. The bottom image illustrates lattice parameters with the ionic radius for $REBaCo_2O_{5+\delta}$, of which the solid symbol indicates oxygen-pressure annealed and the hollow symbol indicates air-synthesized. (c) Resistivity as a function of temperature for oxygen-pressure-annealed $REBaCo_2O_{5+\delta}$. (d) Relationship between the thermoelectric power and temperature of $REBaCo_2O_{5+\delta}$ annealed in oxygen.

value of $|S|$ increases as δ approaches 0.5). Meanwhile, the temperature dependence of S becomes more gradual and abrupt transitions are observed in $DyBaCo_2O_{5+\delta}$ and $HoBaCo_2O_{5+\delta}$, as shown in Fig. S7(b). With an elevation in temperature, a reducing tendency is generally observed for the S of all $REBaCo_2O_{5+\delta}$, and this is in agreement with their negative temperature dependence in resistivity.

Fig. 4(a) shows the powder XRD pattern of $REBaCo_2O_{5+\delta}$ (RE = Pr, Nd, Sm, and Eu) after nitrogen annealing, the process of which results in the broadening of diffraction peaks (see Fig. S5) without introducing secondary phases. The variation in the magnitudes of their lattice parameters was further determined by the Rietveld refinement, as plotted as a function of r_{RE} in Fig. 4(b).

The top image of Fig. 4(b) shows the crystal structure of $RE_LBaCo_2O_{5+\delta}$. On the left is the structural diagram of $RE_LBaCo_2O_{5+\delta}$ synthesized in air, and on the right is the structural diagram of $RE_LBaCo_2O_{5+\delta}$ after nitrogen annealing. After nitrogen annealing, $RE_LBaCo_2O_{5+\delta}$ transitions from the original tetragonal structure to a lower-symmetry orthorhombic structure (similar to the oxygen-annealed $RE_HBaCo_2O_{5+\delta}$). At the same time, the δ value decreases (opposite to the trend observed in oxygen-annealed $RE_HBaCo_2O_{5+\delta}$).

Fig. 4(b) demonstrates the lattice parameters obtained from the Rietveld refinement of $REBaCo_2O_{5+\delta}$ (RE = Pr, Nd, Sm, and Eu) after nitrogen annealing (see more details in Table S4 and Fig. S6). A comparison with the oxygen-annealed and as-sintered samples shows that after annealing, for RE_L (Pr and Nd), the b is significantly larger than $2a$. This causes the original *P4/mmm* space group, obtained by sintering in air, to transition to the lower-symmetry *Pmmm* space group, likely due to oxygen vacancies inducing distortions in the crystal structure. For RE = Sm and Eu, after annealing, the a-axis slightly decreases, while the b-axis slightly increases, leading to a further reduction in

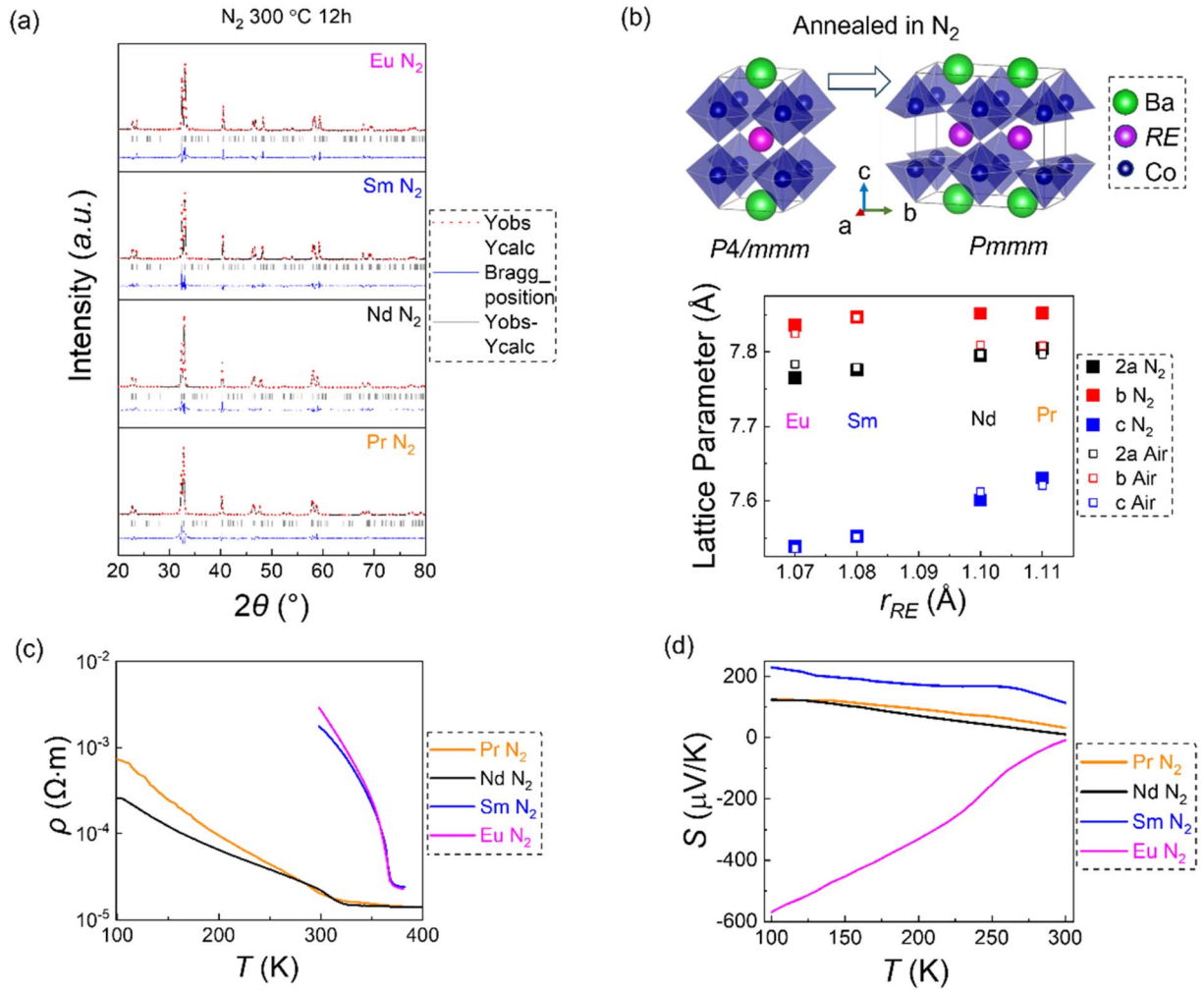

Fig. 4 (a) X-ray diffraction (XRD) patterns for the powder of $REBaCo_2O_{5+\delta}$ annealed in nitrogen for 12 hours at 300 °C. (b) Top image illustrates the crystal structure of $REBaCo_2O_{5+\delta}$ (RE represents rare-earth elements), where RE, Ba, and Co atoms are represented by purple, green, and dark blue, respectively. On the left is a schematic of the structure of $RE_LBaCo_2O_{5+\delta}$ synthesized in air, and on the right is a schematic of the structure of nitrogen-annealed $RE_LBaCo_2O_{5+\delta}$. The bottom figure illustrates the lattice parameter with ionic radius for $REBaCo_2O_{5+\delta}$, of which the solid symbol indicates nitrogen-annealed and the hollow symbol indicates air-synthesized. (c) Resistivity as a function of temperature for the nitrogen-annealed $REBaCo_2O_{5+\delta}$. (d) Temperature dependence of the thermoelectric power in the nitrogen-annealed $REBaCo_2O_{5+\delta}$.

structural symmetry. The *c*-axis remains relatively unchanged before and after annealing for all $REBaCo_2O_{5+\delta}$ compounds.

Fig. 4(c) shows the temperature-dependent resistance (ρ–T) relationship of $REBaCo_2O_{5+\delta}$ (RE = Pr, Nd, Sm, and Eu) after nitrogen annealing. Compared to the samples before annealing, $PrBaCo_2O_{5+\delta}$ and $NdBaCo_2O_{5+\delta}$ exhibit a distinct MIT, as shown in Fig. S6. This is related to the decrease in symmetry of the $REBaCo_2O_{5+\delta}$ structure after nitrogen annealing. The T_{MIT} value for $PrBaCo_2O_{5+\delta}$ is around 290 K, while for $NdBaCo_2O_{5+\delta}$, it is approximately 305 K. After nitrogen annealing, the phase transition of $SmBaCo_2O_{5+\delta}$ and $EuBaCo_2O_{5+\delta}$ becomes sharper, and the temperature of T_{MIT} for the former increases, as shown in Fig. S8. Fig. S9 presents the ρ–T relationship of $RE_MBaCo_2O_{5+\delta}$ (RE = Sm, Eu, Gd, and Tb). Taking $TbBaCo_2O_{5+\delta}$ as an example, a comparison of this material under different annealing conditions reveals that the phase transition is sharpest for the air-sintered sample. After oxygen annealing, the sharpness of the phase transition decreases, and the post-transition resistance is lower. After nitrogen annealing, the MIT disappears, and the material exhibits insulating behavior throughout the temperature range. Overall, oxygen annealing drives $REBaCo_2O_{5+\delta}$ towards metallic behavior, while nitrogen annealing promotes its transition to insulating behavior.

Fig. 4(d) demonstrates the temperature dependence of *S* for $REBaCo_2O_{5+\delta}$ with light and middle rare-earth elements (RE = Pr, Nd, Sm, and Eu) after nitrogen annealing to reduce their oxygen composition. It can be seen that nitrogen annealing converts the magnitude of S from positive to negative for $EuBaCo_2O_{5+\delta}$, indicating the transition in its major carrier type from the hole to the electron. Compared to their air-synthesized counterparts, the magnitude of $|S|$ of all $REBaCo_2O_{5+\delta}$ increases at 100 K and the temperature dependence of *S* becomes more sharp, suggesting that after nitrogen annealing, the δ value approaches 0.5,[17,24,25] as shown in Fig. S7(b).

3.3. Coordinated regulation in the MIT of $REBaCo_2O_{5+\delta}$ from rare-earth substitution and oxygen composition

Fig. 5(a) summarizes the relationship between the T_{MIT} value of $REBaCo_2O_{5+\delta}$ under different annealing conditions and the r_{RE} value. The T_{MIT} value was determined by the temperature with respective to the minima in the tendency $d(\ln \rho)/d(T) - T$, and more details are shown in Fig. S10. It can be seen that the T_{MIT} value generally falls within a narrow range of 290–370 K. This differs from 113-type rare-earth nickelates,[1] cobaltite $RECoO_3$,[2] and A-site ordered oxygen-deficient perovskite $REBaFe_2O_5$,[35] under which conditions the T_{MIT} value can be regulated within wider temperature ranges *via* the r_{RE} value. As shown in Fig. 5(a), the T_{MIT} value shows a maximum for $REBaCo_2O_{5+\delta}$ synthesized in air with RE = Gd, similar to the previous reports.[27] For $REBaCo_2O_{5+\delta}$ with lighter rare-earth compositions (*e.g.*, Sm and Eu), their MITs are more abrupt with the elevated T_{MIT} value upon nitrogen annealing. Similar effects were observed for $REBaCo_2O_{5+\delta}$ with heavier rare-earth compositions (*e.g.*, Dy and Ho), which indicated that MIT behaviors manifest, but upon annealing at MPa-high oxygen pressures.

Fig. 5(b) summarizes the S of $REBaCo_2O_{5+\delta}$ with various RE (*e.g.*, Pr, Nd, Sm, Eu, Gd, Tb, Dy, and Ho) at 100 K. In general, the absolute magnitudes of S are small for air-sintered $REBaCo_2O_{5+\delta}$ with light and middle rare-earth elements (*e.g.*, Pr–Gd), while much larger ones were observed for $REBaCo_2O_{5+\delta}$, *e.g.*, positive S for RE = Tb and Dy, and negative S for RE = Ho. Moreover, the absolute magnitude in the S for $EuBaCo_2O_{5+\delta}$ was enlarged significantly upon nitrogen anneals (see more details in Fig. S11 and S12). According to the previous reports,[17] the magnitude of S can well reflect the oxygen composition (δ) for $REBaCo_2O_{5+\delta}$, and the tendency is summarized in Fig. 5(c) for δ–S. Based on the previously reported δ–S tendency, we further estimate the magnitude of δ for the present $REBaCo_2O_{5+\delta}$ samples. In Fig. 5(d), we further plotted the δ–r_{RE} relationship for $REBaCo_2O_{5+\delta}$ in this work and also those reported previously. The solid symbols represent those showing abrupt MIT behavior, while those with the absence of MIT are indicated by the hollow symbols. It clearly demonstrates that the occurrence of MIT in $REBaCo_2O_{5+\delta}$ is more related to an oxygen stoichiometry approaching 5.5 ($\delta = 0.5$), regardless of the rare-earth composition.

Summarizing all the above-mentioned results highlights two prerequisites for the emergence of MIT behavior in $REBaCo_2O_{5+\delta}$, from the perspectives of both crystal structure and valence. On the one hand, the ground state of $REBaCo_2O_{5+\delta}$ exhibits low crystal symmetry (*e.g.*, adopting the *Pmmm* space group instead of *P4/mmm*), with its lattice constants changing significantly at T_{MIT},[36,37] which indicates strong spin–orbital–lattice coupling. On the other hand, the oxygen composition should be proper to maintain Co^{3+} valence

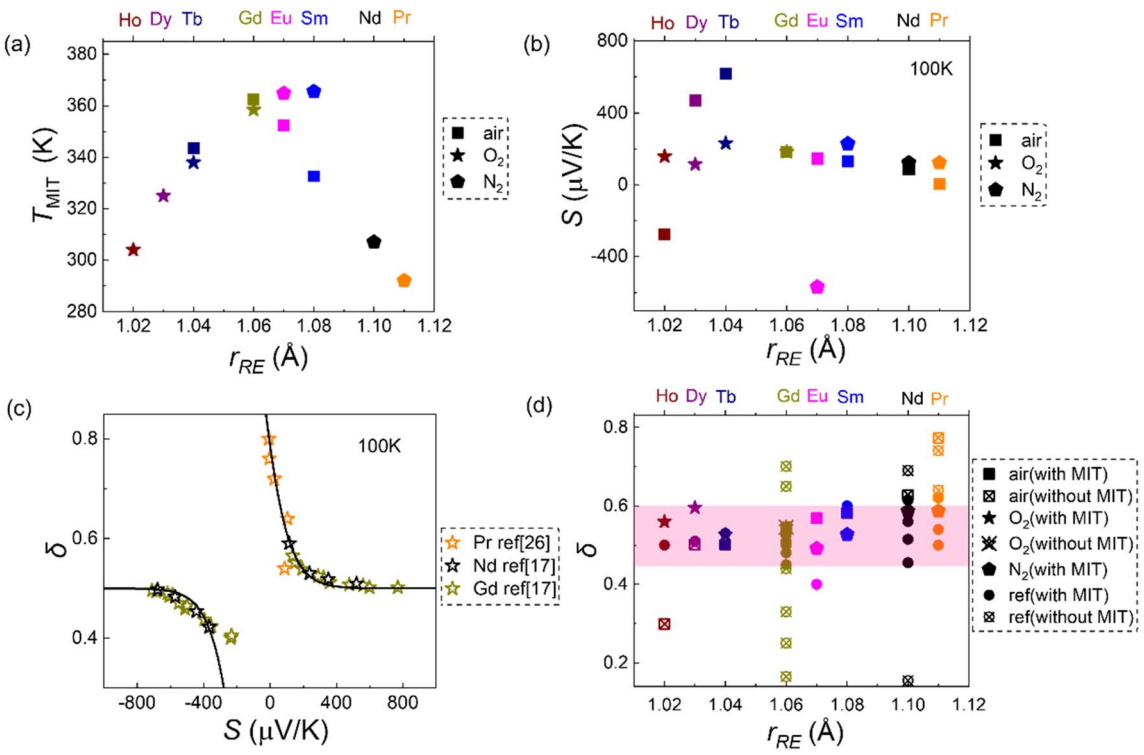

Fig. 5 (a) Metal-insulator transition temperature (T_{MIT}) of the as-prepared $REBaCo_2O_{5+\delta}$ sample, of which the solid symbol indicates air-synthesized, the crosses in the box indicate oxygen-annealed and the hollow symbol indicates nitrogen-annealed. (b) Seebeck coefficient of $REBaCo_2O_{5+\delta}$ at 200 K, of which the solid symbol indicates air-synthesized, the crosses in the box indicate oxygen-annealed and the hollow symbol indicates nitrogen-annealed. (c) Correlation between the oxygen content and the Seebeck coefficient reported in the literature.[17,26] (d) Relationship between the oxygen content and the ionic radius of rare-earth elements, where the oxygen content in this work is calculated based on panel (c) and the points from the literature are also marked in the figure.[17,24,27–34]

states, which is necessary to sustain the high-/low-spin-state transitions for $REBaCo_2O_{5+\delta}$ (see more details in Fig. S13). The necessity to satisfy both prerequisites limits the tunability of the MIT behavior of the double perovskite system $REBaCo_2O_{5+\delta}$ in contrast to the 113-type perovskite cobaltite.

4. Conclusions

In conclusion, we demonstrate that the occurrence of an abrupt MIT in $REBaCo_2O_{5+\delta}$ relies on the synergistic coordination between the RE ionic radius-induced CoO_6 octahedral distortion and the oxygen vacancy-modulated Co valence state to reach a low structural symmetry, with δ approaching 0.5. From the cationic perspective, the e transportation behavior of $REBaCo_2O_{5+\delta}$ synthesized in air gradually shifts from the metal to the insulator along the lanthanide series from Pr to Ho, with the occurrence of the MIT for RE in the middle (*e.g.*, Sm, Eu, Gd and Tb). From the anionic perspective, the MIT was able to be further extended to more RE compositions from the anionic perspective by annealing the insulating $REBaCo_2O_{5+\delta}$ (RE: Dy and Ho) or metallic $REBaCo_2O_{5+\delta}$ (RE: Pr and Nd) at MPa-high oxygen or nitrogen pressure, respectively. Further estimation of the oxygen composition *via* their magnitude of thermopower indicates that their MIT behaviors coincide with a narrow distribution of δ around 0.5 and the descendent structural symmetry towards *Pmmm* from *P*4/*mmm*. This unveils the distinctiveness in spin-state transition-driven MIT compared to the Bloch–Wilson, Mott, or Peierls transitions, providing a versatile platform for fundamental explorations beyond ordinary correlated systems.

Conflicts of interest

We declare no competing financial interest.

Data availability

The data that support the findings of this study are available from the corresponding author upon reasonable request.

Supplementary information (SI) is available. See DOI: https://doi.org/10.1039/d6ra00137h.

Acknowledgements

This work was supported by the National Key Research and Development Program of China (No. 2021YFA0718900), the National Natural Science Foundation of China (No. 62474017), and the Beijing Nova Program Interdisciplinary Cooperation Project (No. 20240484581). We also thank the 4B9B station at the Beijing Synchrotron Radiation Facility (BSRF).

References

1 Z. Li, *et al.*, Metal-to-insulator transition and stability for metastable correlated perovskite nickelates with complex RE-composition, *J. Am. Ceram. Soc.*, 2025, **108**(10), e70064.
2 F. Zhang, *et al.*, Molten salt synthesis of metastable perovskite cobaltites with high-temperature metal to insulator transitions, *J. Alloys Compd.*, 2025, **1034**, 181307.
3 Y. X. Xia, *et al.*, Metal-to-insulator transition in platinum group compounds, *Rare Met.*, 2024, **43**(8), 3460–3474.
4 F. y. Li, *et al.*, Bulk superconductivity up to 96 K in pressurized nickelate single crystals, *Nature*, 2026, **649**, 871–878.
5 Y. He, *et al.*, Rapid change of superconductivity and electron-phonon coupling through critical doping in Bi-2212, *Science*, 2018, **362**(6410), 62–65.
6 T. Fix, *et al.*, Sensitive Bandgap Reduction of $SrTiO_3$ through Incorporation of Sulfur Using Ion Implantation, *Sol. RRL*, 2024, **8**(12), 2400237.
7 N. I. Solin, *et al.*, Spin States of Cobalt Ions and a Metal–Semiconductor Transition in Layered Cobaltites $PrBaCo_2O_{5+\delta}$ (δ = 0.52, 0.74), *J. Exp. Theor. Phys.*, 2023, **137**(5), 664–674.
8 E. Marelli, *et al.*, Correlation between Oxygen Vacancies and Oxygen Evolution Reaction Activity for a Model Electrode: $PrBaCo_2O_{5+\delta}$, *Angew. Chem., Int. Ed.*, 2021, **60**(26), 14609–14619.
9 F. Jin, *et al.*, Enhancing Oxygen Reduction Activity and CO_2 Tolerance by a Bismuth Doping Strategy for Solid Oxide Fuel Cell Cathodes, *Adv. Funct. Mater.*, 2024, **34**(29), 2400519.
10 J. Dąbrowa, *et al.*, High-entropy approach to double perovskite cathode materials for solid oxide fuel cells: Is multicomponent occupancy in (La,Pr,Nd,Sm,Gd)$BaCo_2O_{5+\delta}$ affecting physicochemical and electrocatalytic properties?, *Front. Energy Res.*, 2022, **10**, 899308.
11 T. V. Aksenova, *et al.*, Crystal structure and physicochemical properties of layered perovskite-like phases $LnBaCo_2O_{5+\delta}$, *Russ. J. Phys. Chem. A*, 2011, **85**(3), 427–432.
12 Y. Lu, *et al.*, Specific features of spectral and electrical properties of double-perovskite $LnBaCo_2O_{5+\delta}$ (Ln=lanthanides) under solar irradiation, *Ceram. Int.*, 2017, **43**(1), 1186–1192.
13 I. O. Troyanchuk, *et al.*, Magnetic and electrical transport properties of orthocobaltites $R_{0.5}Ba_{0.5}CoO_3$ (R = La, Pr, Nd, Sm, Eu, Gd, Tb, Dy), *Phys. Rev. B:Condens. Matter Mater. Phys.*, 1998, **58**(5), 2418–2421.
14 A. Maignan, *et al.*, Structural and Magnetic Studies of Ordered Oxygen-Deficient Perovskites $LnBaCo_2O_{5+\delta}$, Closely Related to the "112" Structure, *J. Solid State Chem.*, 1999, **142**(2), 247–260.
15 P. Karen, Chemistry and thermodynamics of the twin charge-ordering transitions in $RBaFe_2O_{5+w}$ series, *J. Solid State Chem.*, 2004, **177**(1), 281–292.
16 T. Dasgupta, *et al.*, A novel method to control oxygen stoichiometry and thermoelectric properties in (RE)$BaCo_2O_{5+\delta}$, *Bull. Mater. Sci.*, 2008, **31**(6), 859–862.
17 A. A. Taskin, *et al.*, Origin of the large thermoelectric power in oxygen-variable $RBaCo_2O_{5+x}$ (R=Gd,Nd), *Phys. Rev. B:Condens. Matter Mater. Phys.*, 2006, **73**(12), 121101.
18 H. Kusuya, *et al.*, Structural Change at Metal-Insulator Transition of $Tb_2Ba_2Co_4O_{11}$, *J. Phys. Soc. Jpn.*, 2001, **70**, 3577–3580.

19 T. V. Aksenova, *et al.*, Oxygen nonstoichiometry, thermal expansion and high-temperature electrical properties of layered $NdBaCo_2O_{5+\delta}$ and $SmBaCo_2O_{5+\delta}$, *Mater. Res. Bull.*, 2010, **45**(9), 1288–1292.

20 S. Li, *et al.*, Phosphatizing Engineering of Perovskite Oxide Nanofibers for Hydrogen Evolution Reaction to Achieve Extraordinary Electrocatalytic Performance, *Adv. Funct. Mater.*, 2022, **32**(26), 2112164.

21 V. R. Galakhov, *et al.*, Effects of Nonstoichiometry and Plastic Deformation on Charge and Spin States of Cobalt Ions in $LnBaCo_2BaO_{5.5-\delta}$ (Ln = Tb, Eu): Soft X-ray Absorption Spectroscopy Studies, *Phys. Met. Metallogr.*, 2019, **120**(13), 1354–1358.

22 Z. Hu, *et al.*, Different Look at the Spin State of Co^{3+} Ions in a CoO_5 Pyramidal Coordination, *Phys. Rev. Lett.*, 2004, **92**(20), 207402.

23 J.-M. Chen, *et al.*, A Complete High-to-Low spin state Transition of Trivalent Cobalt Ion in Octahedral Symmetry in $SrCo_{0.5}Ru_{0.5}O_{3-\delta}$, *J. Am. Chem. Soc.*, 2014, **136**(4), 1514–1519.

24 H. D. Zhou, *et al.*, Metamagnetism in $DyBaCo_2O_{5+x}$, $x \approx 0.5$, *J. Solid State Chem.*, 2004, **177**(10), 3339–3345.

25 A. A. Taskin, *et al.*, Electron-Hole Asymmetry in $GdBaCo_2O_{5+x}$: Evidence for Spin Blockade of Electron Transport in a Correlated Electron System, *Phys. Rev. Lett.*, 2005, **95**(17), 176603.

26 B. Rivas-Murias, *et al.*, Influence of the oxygen content and the preparation method on the power factor of $PrBaCo_2O_{5+\delta}$ samples ($0.54 \leq \delta \leq 0.84$), *J. Alloys Compd.*, 2011, **509**(17), 5250–5255.

27 P. Miao, *et al.*, Hole-doping-induced melting of spin-state ordering in $PrBaCo_2O_{5.5+x}$, *Phys. Rev. B*, 2017, **95**(12), 125123.

28 T. Saito, *et al.*, Optical Study of Metal-Insulator Transition in $SmBaCo_2O_{6-\delta}$ Single Crystal, *J. Phys. Soc. Jpn.*, 2000, **69**(11), 3525–3528.

29 C. Martin, *et al.*, Magnetoresistance in the oxygen deficient $LnBaCo_2O_{5.4}$ (Ln=Eu, Gd) phases, *Appl. Phys. Lett.*, 1997, **71**(10), 1421–1423.

30 A. A. Taskin, *et al.*, Transport and magnetic properties of $GdBaCo_2O_{5+x}$ single crystals: A cobalt oxide with square-lattice CoO_2 planes over a wide range of electron and hole doping, *Phys. Rev. B:Condens. Matter Mater. Phys.*, 2005, **71**, 134414.

31 A. Podlesnyak, *et al.*, Magnetic and electric transport properties of $TbBaCo_2O_{5.5}$ single crystal, *J. Magn. Magn. Mater.*, 2007, **316**(2), e710–e712.

32 Y. Moritomo, *et al.*, Metal-insulator transition induced by a spin-state transition in $TbBaCo_2O_{5+\delta}$ ($\delta = 0.5$), *Phys. Rev. B:Condens. Matter Mater. Phys.*, 2000, **61**(20), R13325–R13328.

33 T. Fujita, *et al.*, Anomalous Hall Resistivity of $TbBaCo_2O_{5.53}$ with Nontrivial Magnetic Structure, *J. Phys. Soc. Jpn.*, 2006, **75**, 114710.

34 A. Maignan, *et al.*, Thermoelectric Power of $HoBaCo_2O_{5.5}$: Possible Evidence of the Spin Blockade in Cobaltites, *Phys. Rev. Lett.*, 2004, **93**(2), 026401.

35 Y. Yu, *et al.*, Metal-to-insulator transitions in 3d-band correlated oxides containing Fe compositions, *Int. J. Miner., Metall. Mater.*, 2024, **31**(1), 48–59.

36 E. Pomjakushina, *et al.*, Orbital order-disorder transition with volume collapse in $HoBaCo_2O_{5.5}$: A high-resolution neutron diffraction study, *Phys. Rev. B:Condens. Matter Mater. Phys.*, 2006, **73**(11), 113105.

37 J. E. Jørgensen, *et al.*, Magnetic ordering in $HoBaCo_2O_{5.5}$, *Phys. Rev. B:Condens. Matter Mater. Phys.*, 2008, **77**(2), 024427.